Measurement of K_{e3} Semileptonic Form Factor Slope and Curvature and Pole in the Decay $K_L \to \pi^{\pm} e^{\mp} \nu$ at KLOE

M. Antonelli, M. Dreucci, C. Gatti

INFN Laboratori Nazionali di Frascati

Abstract

We present the measurement of the $K - \pi$ vector current parameters in the decay $K_L \to \pi^{\pm} e^{\mp} \nu$. We use 328 pb^{-1} of data collected in 2001 and 2002, corresponding to $\sim$ 2 million of K_{e3} events. Measurements of semileptonic form factors provide information about the dynamics of strong interaction and are necessary to evaluate the phase-space integral I_K^e, needed to measure the CKM matrix element $|V_{us}|$ from $K_L \to \pi^{\pm} e^{\mp} \nu$. Our result is $\lambda'_+ = (28.6 \pm 0.5 \pm 0.4)10^{-3}$ for a linear fit, and $\lambda'_+ = (25.5 \pm 1.5 \pm 1.0)10^{-3}$, $\lambda''_+ = (1.4 \pm 0.7 \pm 0.4)10^{-3}$ for a quadratic fit.

1 Introduction

Semileptonic kaon decays, $K_L \to \pi^{\pm} \ell^{\mp} \nu$, (Fig. 1) offer possibly the cleanest way to obtain an accurate value of the Cabibbo angle or better V_{us}. Since the $K \to \pi$ is a $0^- \to 0^-$ transition, only the vector part of the weak current has a non vanishing contribution. They are therefore protected by the Ademollo-Gatto theorem against SU(3) breaking corrections to lowest order. The biggest uncertainty at present, in going from decay rate to V_{us}, is due to the difficulties in computing the matrix element $\langle \pi | j_\alpha | K \rangle$. The electron mode $K_L \to \pi^{\pm} e^{\mp} \nu$

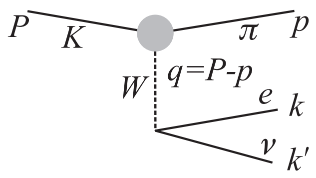

Fig. 1. Amplitude for $K_L \to \pi^{\pm} \ell^{\mp} \nu$. The grey region indicates the $K \to \pi W$ vertex structure.

is easier to measure and only one form factor is involved. P, p, k and k' are the kaon, pion, electron and neutrino momenta, respectively. Throughout this paper, m is the mass of the charged pion and M that of the neutral kaon. Terms in $(P - p)_\alpha$ which acquire an m_e factor are neglected. Therefore:

$$\langle \pi | J_\alpha^V | K \rangle = f_+(t)(P + p)_\alpha$$

We replace the form factor above with $f_+(0) \times \hat{f}_+(t)$, where $t = (P-p)^2 = (k+k')^2 = M^2 + m^2 - 2ME_\pi$ is the only L-invariant variable and $\hat{f}_+(0) = 1$. The form factor is dominated by the vector $K - \pi$ resonances, the closest being the $K^*(892)$. Note that for $t > 0$, $\hat{f}_+(t) > 1$. The presence of the form factor increases the value of the phase space integral and the decay rate. The natural form for $\hat{f}(t)$ is:

$$\hat{f}_+(t) = \frac{M_V^2}{M_V^2 - t}. \tag{1}$$

It is also customary to expand the form factor as:

$$\hat{f}_+(t) = 1 + \lambda'_+ \, \frac{t}{m^2} + \frac{1}{2}\, \lambda''_+ \left(\frac{t}{m^2}\right)^2 + \ldots \tag{2}$$

In the following we retain liner and quadratic terms. Note that an expansion of the pole form above gives $\lambda'_+ = (m/M_V)^2$ and $\lambda''_+ = 2 \times {\lambda'_+}^2$. From $P + p = 2P - (k + k')$, neglecting the $k + k'$ term also $\propto m_e$, the amplitude is:

$$\mathfrak{M} = \langle \pi e \nu | H_W | K \rangle = 2\frac{V_{us} G_F f_+(0)}{\sqrt{2}} P_\alpha \bar{u}(k)\gamma^\alpha(1-\gamma^5)u(k')\hat{f}_+(t). \tag{3}$$

Squaring, summing over spins and integrating over all variables but the pion energy we get the pion spectrum

$$g(z) \propto \left(z^2 - 4\,\alpha\right)^{\frac{3}{2}} \left(1 + \frac{\lambda'_+}{\alpha}\,(\xi - z) + \frac{\lambda''_+}{2\,\alpha^2}\,(\xi - z)^2\right)^2$$

where $\alpha = m^2/M^2$, $\xi = 1 + \alpha$ and $z = 2\,E_\pi/M$ is the normalized pion energy. The spectrum can also be written in terms of $t = m^2(\xi - z)/\alpha$ as

$$\begin{aligned} &h(t) \propto \lambda^{3/2} \hat{f}_+(t)^2 \\ &\quad \lambda = t^2 + M^4 + m^4 - 2\,t\,M\,2 - 2\,t\,m^2 - 2\,M\,m \end{aligned} \tag{4}$$

In Fig. 2 is shown the $h(t)$ distribution for different values of the slope parameters. Distortions of the t-distribution must be kept under tight control. A distortion of the spectrum linear in t like $\sim 1 + \alpha\, t$ produces shifts ($\delta\lambda'_+/\lambda'_+ \sim 20\,\alpha$, $\delta\lambda''_+/\lambda''_+ \sim 10\,\alpha$). The 328 pb^{-1} of data used in this analysis, taken in 2001 and 2002, are divided in 14 periods of about 25 pb^{-1}. For each data period we have the corresponding Monte Carlo simulation period with about the same statistic.

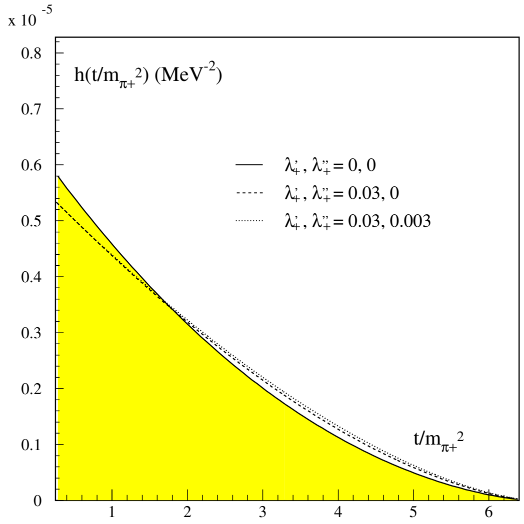

Fig. 2. K_{e3} t distribution as a function of λ'_+ and λ''_+.

2 Event Selection

We tag K_L by detecting $K_S \to \pi^+\pi^-$ decays close to the interaction point and clusters from K_S decay associated to fired trigger sectors of calorimeter. To select K_L decays we accept all events with two tracks of opposite curvature forming a vertex in a fiducial volume. To remove background from $K_L \to \pi^+\pi^-\pi^0$, $K_L \to \pi^+\pi^-$ and $K_L \to \pi^\pm\mu^\mp\nu$ decays we apply kinematic cuts. After these cuts a not negligible background from $K_L \to \pi^\pm\mu^\mp\nu$ still remains. To remove it we use time of flight to identify electrons.

2.1 Tagging

The K_L tagging algorithm is fully described in Ref. 1 and only the relevant aspects will be given in the following. Candidate events are identified by the presence of a $K_S \to \pi^+\pi^-$ decay. We require a vertex with two tracks of opposite curvature with origins within a cylindrical fiducial volume of radius $r_{xy} < 10$ cm and length $\Delta z < 20$ cm, centered on the collision region, as determined for each run using Bhabha events. The two-track invariant mass, in the pion mass hypothesis for both tracks, must be within 5 MeV of m_{K^0} . The magnitude of the total momentum of the two tracks must be within 10 MeV of the value expected from two-body ϕ decay kinematics and the value of $\mathbf{p}_\phi$. If more than one vertex satisfies these criteria, that closest to the nominal ϕ vertex position is identified as the $K_S \to \pi^+\pi^-$. The K_L momentum, p_{K_L}, is obtained from the kinematics of the $\phi \to K_S K_L$ decay, using the K_S direction reconstructed from the measured momenta of the decay tracks and the known value of $\mathbf{p}_\phi$. The resolution is dominated by the beam-energy spread, and amounts to about 0.8 MeV/c. The position of the ϕ production point, $\mathbf{x}_\phi$, is determined as the point of closest approach of the K_S momentum, propagated backward from the K_S vertex, to the beam line. The K_L line of flight (*tagging line*) is then constructed from the K_L momentum, $\mathbf{p}_{K_L} = \mathbf{p}_\phi - \mathbf{p}_{K_S}$, and the position of the production vertex, $\mathbf{x}_\phi$.

As described in Ref. 1, the tagging procedure is not perfect, because it's efficiency depends slightly on the evolution of the K_L. We include events in which the K_L interacts in the calorimeter, escapes the detector, or decays to any final state. The difference in tagging efficiency in each case depends on the tagging algorithm; the minimization of such differences is used to optimize the tagging criteria. The main source of the difference in the tagging efficiency is induced from dependence of the trigger efficiency on the K_L behavior. Therefore, it is fundamental to know whether the K_S alone can satisfy the calorimeter trigger in order to reduce this effect. To identify events in which the K_S alone satisfies the calorimeter trigger, we require the presence of two clusters from the $K_S \to \pi^+\pi^-$ decay associated with fired trigger sectors (*autotrigger*). We determine the event t_0 using the clusters from the K_S.

2.2 Extrapolation of tracks to the calorimeter

For the purposes of track-to-cluster association, we define two quantities related to the distance between the track, extrapolated at the entry point of the calorimeter, and the closest cluster: $\mathrm{d_{TC}}$, the distance from the extrapolated entry point on the calorimeter to the cluster centroid and $\mathrm{d_{tc\perp}}$, the component of this distance in the plane transverse to the momentum of the track at the impact position. The distribution of this last variable is shown in Fig. 3 for data and Monte Carlo. We only consider clusters with $\mathrm{d_{tc\perp}} < 30$ cm and $E >50$ MeV. If there is more than one candidate, we use the cluster for which $\mathrm{d_{tc\perp}}$ is smaller.

2.3 Extrapolation of K_L Decay Tracks

All tracks in the chamber, after removal of those from the K_S decay and their descendants, are extrapolated to their points of closest approach to the *tagging line*. For each track candidate, we evaluate the point of closest approach to the *tagging line*, $\mathbf{x}_\mathrm{c}$, and the distance of closest approach, d_c. The momentum $\mathbf{p}_\mathrm{c}$ of the track at $\mathbf{x}_\mathrm{c}$ and the extrapolation length, l_c, are also computed. Tracks satisfying $d_\mathrm{c} < ar_{xy} + b$, with $a = 0.03$ and $b = 3$ cm, and -20 cm $< l_\mathrm{c} < 25$ cm are accepted as K_L decay products, being $r_{xy}$the distance of the vertex in

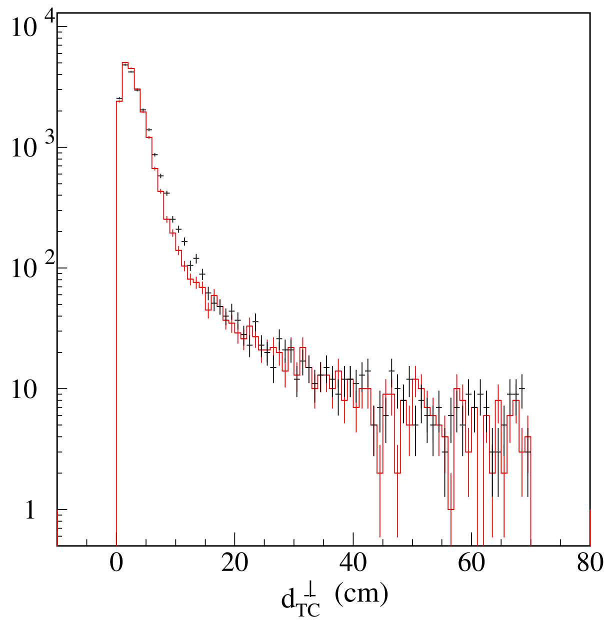

Fig. 3. Plot of $d_{tc\perp}$ in barrel ECAL for Monte Carlo (solid line) and Data(dots).

the transverse plane. For each sign of charge we consider as associated to the K_L decay the track with the smallest value of d_c. Starting from these track candidates a vertex is reconstructed. The events are retained if the vertex is in the fiducial volume $35 < r_{xy} < 150$ cm and $|z| < 120$ cm. Measured momenta have been smeared for Monte Carlo events as described in Ref. 1 to improve the agreement with data.

2.4 Kinematic based event selection

To remove background from $K_L \to \pi^+\pi^-\pi^0$ and $K_L \to \pi^+\pi^-$ with minimal efficiency loss we apply a set of loose kinematic cuts: assuming the two tracks belong to pions, we require

$$E^2_{miss} - p^2_{miss} - M^2_{\pi^0} < -5000 \;\; \mathrm{MeV}^2 \tag{5}$$

and

$$\sqrt{E^2_{miss} + p^2_{miss}} > 10\,\mathrm{MeV}, \tag{6}$$

respectively, where E_{miss} and p_{miss} are the missing energy and momentum. The distributions of $E^2_{miss} - p^2_{miss} - M^2_{\pi^0}$ and $\sqrt{E^2_{miss} + p^2_{miss}}$ obtained from Monte Carlo are shown in Fig. 2.4 for the signal and for the background. After these cuts the efficiency remains close to 1 while the background rejection is about 90%.

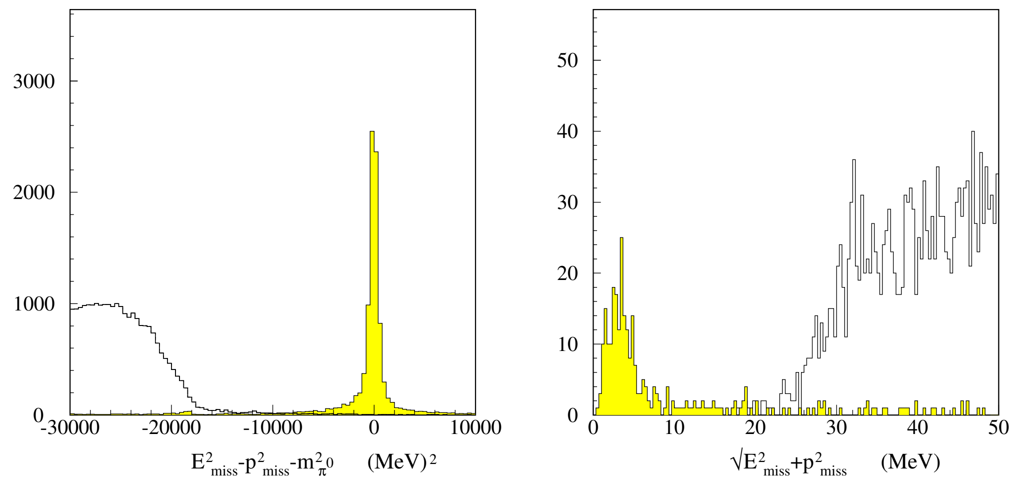

(a) $K_L \to \pi^+\pi^-\pi^0$ events (b) $K_L \to \pi^+\pi^-$ events

Fig. 4. Monte Carlo, kinematic cuts. In both cases we assume the pion mass for each track. Signal solid, background filled.

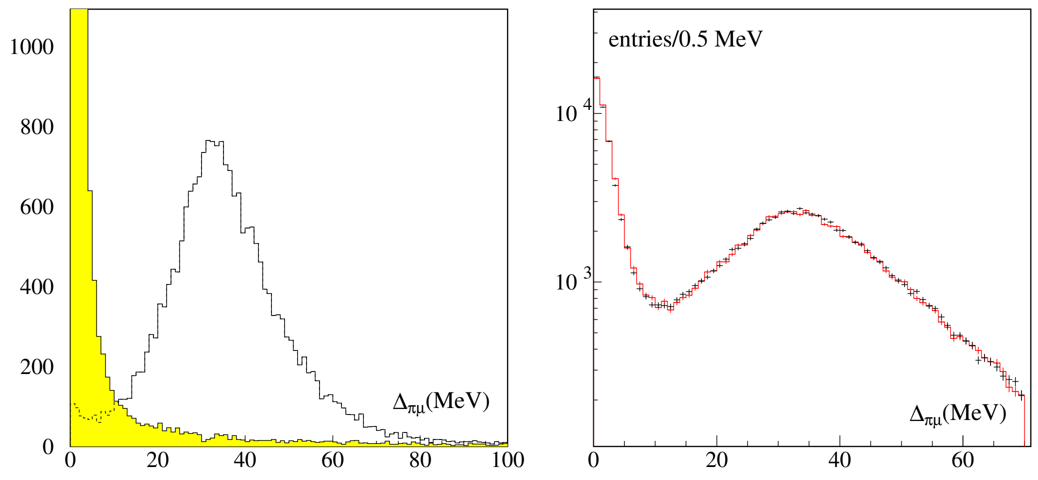

(a) Monte Carlo (b) Data-Mc comparison

Fig. 5. (a) Monte Carlo: $\Delta_{\pi\mu}$ distribution for $K_L \to \pi^\pm\mu^\mp\nu$ (background, filled) and $K_L \to \pi^\pm e^\mp\nu$ (signal, solid). (b) Comparison Data-MC for $K_L \to \pi^\pm\ell^\mp\nu$.

A large amount of background from $K_L \to \pi^\pm\mu^\mp\nu$ has been rejected using $\Delta_{\pi\mu}$, the lesser between $|E_{miss} - p_{miss}|$ in the two hypothesis, $\pi\mu$ or $\mu\pi$. The distribution of $\Delta_{\pi\mu}$ obtained from Monte Carlo is shown in Fig. 2.4 for signal and background. We retain events only if this variable is greater than 10 MeV. The use of $\pi\mu$ hypothesis is more effective than the πe hypothesis: in the former we have an efficiency of $\sim$ 97% with a contamination of $\sim$ 10%, in the latter an efficiency of $\sim$ 85% and a contamination of $\sim$ 6.5%. After all kinematic cuts the efficiency is about 96%.

The kinematic event selection does not remove the background from $K_L \to \pi e\nu$ with opposite charge sign and from $K_L \to \pi^{\pm}\mu^{\mp}\nu$ decay at the desired level. The total background contamination is about $\sim 12\%$, almost entirely due to $K_L \to \pi^{\pm}\mu^{\mp}\nu$. Since the fit result is very sensitive to the amount of background, we make use of the time of flight (ToF) information to further reduce the contamination. Track-to-cluster association is performed as described in Sec. 2.2. We define for the $i^{\rm th}$ track coming from the K_L vertex and associated to a cluster:

$$\Delta t_i = t_{\rm cl} - t_{\rm exp},\\ i = \pi^+, \pi^-, e^+, e^-$$

in which $t_{\rm cl}$ is the cluster time and $t_{\rm exp}$ is the expected time of flight, evaluated

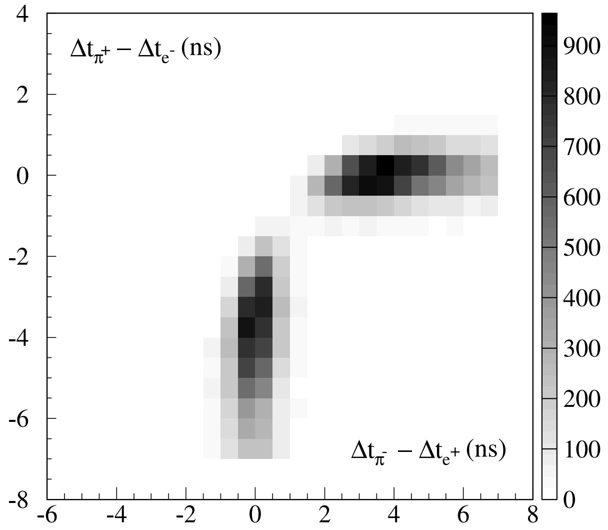

Fig. 6. Distribution of $\Delta t_{\pi^+} - \Delta t_{e^-}$ vs $\Delta t_{\pi^-} - \Delta t_{e^+}$ for Monte Carlo signal events

according to a well defined mass hypothesis. In the evaluation of $t_{\rm exp}$ we also include the time from the impact point to the cluster centroid distribution as in Ref. 2.

An effective way to select the correct charge assignment, πe or $e\pi$, is obtained by choosing the lesser between $|\Delta t_{\pi^+} - \Delta t_{e^-}|$ and $|\Delta t_{\pi^-} - \Delta t_{e^+}|$. The plot of Fig. 6 shows a net separation for the two cases. After the charge assignment we consider the variables $\Delta t_\pi + \Delta t_e$ and $\Delta t_\pi - \Delta t_e$. The scatter plot of $\Delta t_\pi - \Delta t_e$ vs $\Delta t_\pi + \Delta t_e$ obtained from Monte Carlo is shown in Fig. 7 for the signal and the background. The choice of this combination derives from the different contribution to the resolution (0.5 ns for the former, 0.4 ns for the latter). We select signal by using the 2σ elliptic cut shown in Fig. 7 with an efficiency of about 70%. After the ToF cut we have a contamination of ∼0.7%, almost

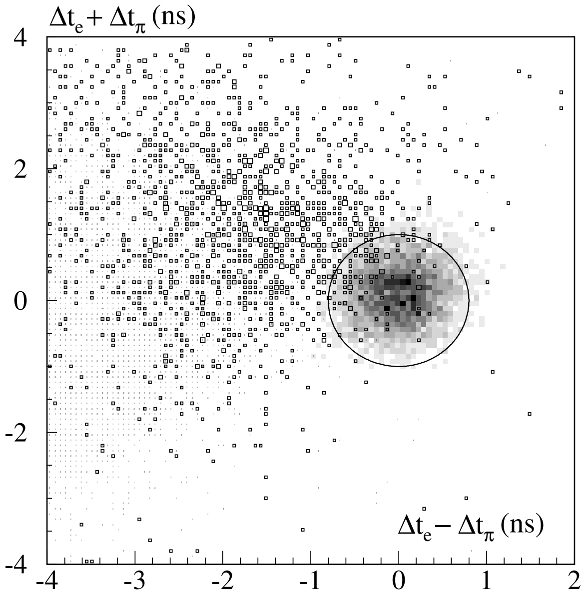

Fig. 7. Monte Carlo: $\Delta t_e + \Delta t_\pi$ versus $\Delta t_e - \Delta t_\pi$. Signal (gray scale), background from opposite sign (dot), background from $K_L \to \pi^\pm \mu^\mp \nu$ same sign (box).

entirely due to $K_L \to \pi^\pm \mu^\mp \nu$ decay. The ratio $S/(S+B)$ after this cut is shown in Fig. 8 as a function of t.

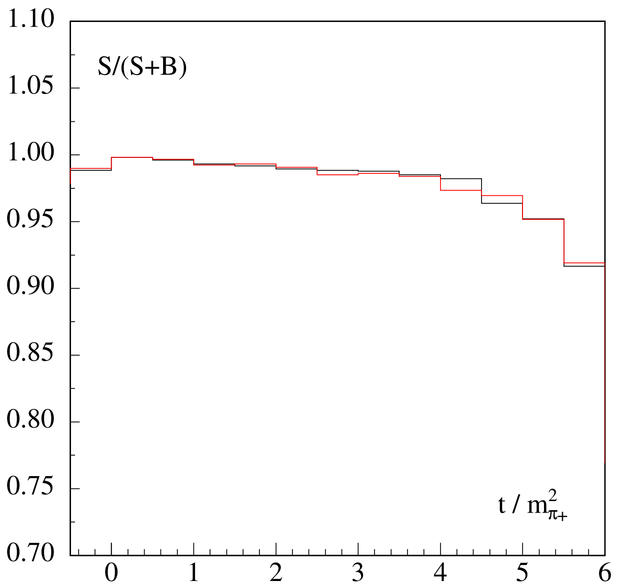

Fig. 8. Signal purity: S/S+B ratio for the two charged decays.

3 Efficiency evaluation

The total efficiency:

$$\epsilon_{tot} = \epsilon_{rec}(t) \times \epsilon_{kine}(t) \times \epsilon_{tof}(t) \tag{7}$$

is given by the product of the efficiencies for the reconstruction, $\epsilon_{rec}(t)$, which includes the tagging, the tracking, and the clustering requirements, for the kinematic event selection, $\epsilon_{kine}(t)$, and for the ToF event selection, $\epsilon_{tof}(t)$. All reconstruction efficiencies are directly evaluated from data control samples and folded with the expected kinematic distributions from Monte Carlo with the exception of the tagging efficiency that has been evaluated from Monte Carlo. The efficiency for the kinematic and ToF event selections are evaluated from Monte Carlo where data driven corrections have been implemented.

3.1 Tagging efficiency

For tagging K_L we require the presence of two clusters from $K_S \to \pi^+\pi^-$ associated with fired trigger sector (*autotrigger*). The tag efficiency has been obtained form Monte Carlo. Fig. 9 shows that tag efficiency is about 40 % and it is independent on t within 0.4%.

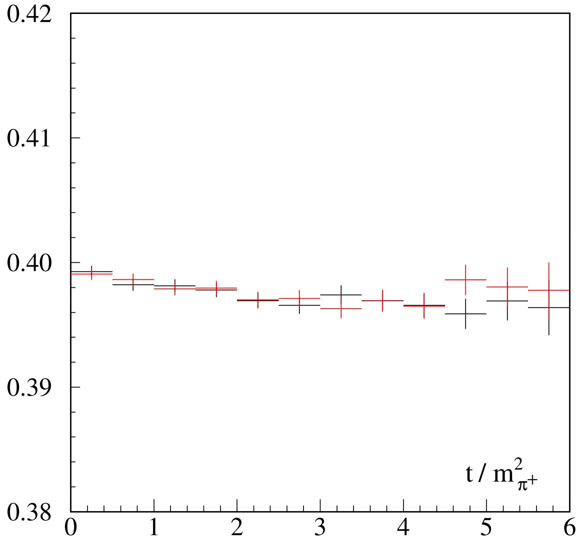

Fig. 9. Tagging efficiency from Monte Carlo. $K_L \to \pi^+e^-\nu$ in black, $K_L \to \pi^-e^+\nu$ in red. Full statistic.

3.2 Tracking and vertex efficiency

The tracking efficiency is determined by counting the number of events in which there is at least a K_L decay track and the number of events in which there are two decay tracks of opposite sign (see Ref. 1). The data-MC difference in the single-to-double ratio is then used to correct the MC estimate for the tracking efficiency. This correction is evaluated as a function of the track momentum using $K_L \to \pi^+\pi^-\pi^0$ and $K_L \to \pi^\pm e^\mp \nu$ events. In $K_L \to \pi^+\pi^-\pi^0$ events, the momentum of one decay track is calculated with a resolution of about 10 MeV using the two photons from the π^0 decay, the momentum of the other decay track and the K_L momentum. In order to obtain the correction for higher momentum tracks (above ~ 150 MeV), $K_L \to \pi^\pm e^\mp \nu$ decays are used, in which the electrons are identified by time of flight with a purity of $\sim$95%. The momentum of the second K_L track is evaluated from the missing energy with a resolution of about 30 MeV. To select $K_L \to \pi^+\pi^-\pi^0$ events, we require at least one K_L decay track and two photons from the π° decay. To reject background, cuts are applied on the two-photon invariant mass and on the times of flight of the photons. The vertex efficiency is the ratio of the

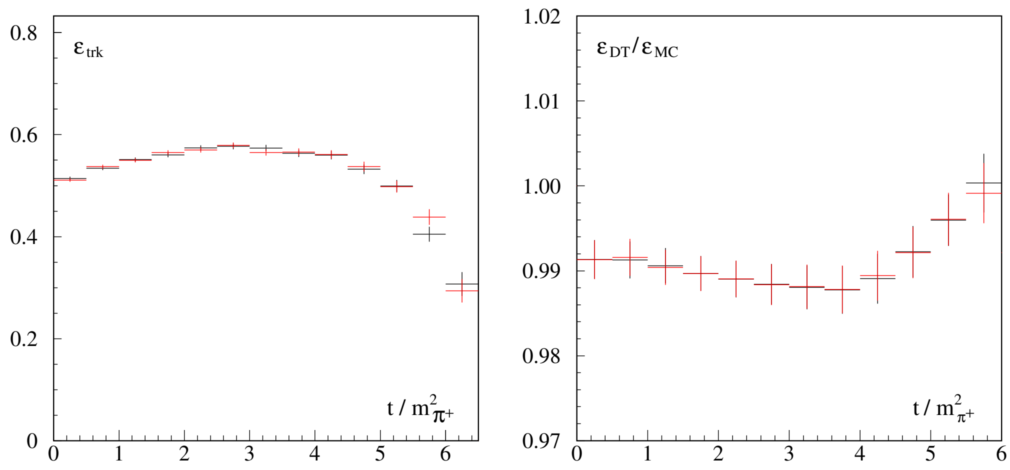

(a) (b)

Fig. 10. $K_L \to \pi^+ e^- \nu$ in black, $K_L \to \pi^- e^+ \nu$ in red. The plot refers to a single period. (a) Tracking efficiency from Monte Carlo. (b) Correction to tracking efficiency from control sample.

number of events with at least two K_L decay tracks of opposite charge that form a vertex to the number of events with at least two K_L decay tracks of opposite charge. As shown in Fig. 3.2, the vertex efficiency is close to 1, and the values obtained from Monte Carlo are in agreement with those from data to within 0.1%.

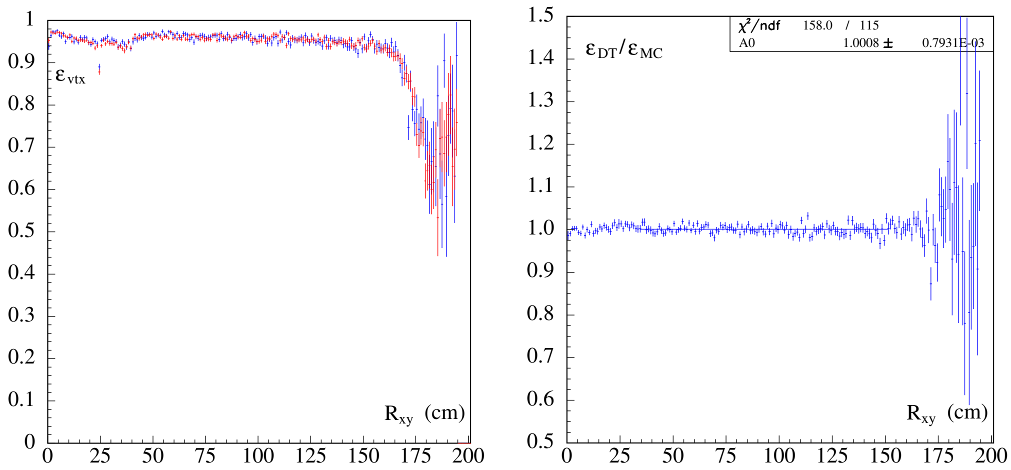

Fig. 11. Left: Vertex efficiency as a function of the transverse radius for data (blue) and Monte Carlo (red). Right: Data-Monte Carlo ratio of vertex efficiencies as a function of the transverse radius.

3.3 Track-to-cluster efficiency

The track-to-cluster efficiency has been evaluated from a pure sample of electrons and pions from K_{e3} selected by means of kinematics and independent calorimeter informations. The data-MC difference in the efficiency obtained from the control sample is used to correct the MC estimate for the track-to-cluster efficiency. Kinematics is used to select K_{e3} with a purity of about of 98%: the lesser between $\Delta_{\pi e} = |E_{miss} - p_{miss}|$ in the two hypothesis, πe or $e\pi$, is required to be smaller than 5 MeV (see Fig. 12).

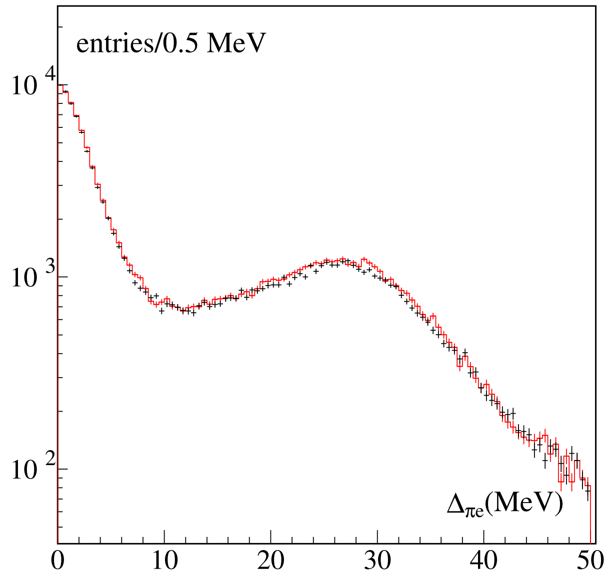

Fig. 12. Comparison Data-MC: $\Delta_{\pi e}$ distribution for $K_L \to \pi^{\pm}\ell^{\mp}\nu$.

$K_L \to \pi^+ e^- \nu$ events are separated from $K_L \to \pi^- e^+ \nu$ events using the following estimator :

$$y_{rec} = \frac{|M_\ell^2(e,\pi) - M_e^2|^{1.5} - |M_\ell^2(\pi,e) - M_e^2|^{1.5}}{max|M_\ell^2 - M_e^2|^{1.5}} \tag{8}$$

in which $M_\ell^2(i,j)$ is the lepton squared invariant mass reconstructed with the two mass hypotheses, πe or $e\pi$, obtained from:

$$M_\ell^2 = (p_K - p_\pi - p_{miss})^2$$
$$E_{miss} = |p_{miss}|$$

in which we assume a zero mass for neutrino. The choice of the 1.5 value for the exponent is the most effective, as results from Monte Carlo. In Fig. 3.3 the distribution of this variable for signal and background is shown. We cut

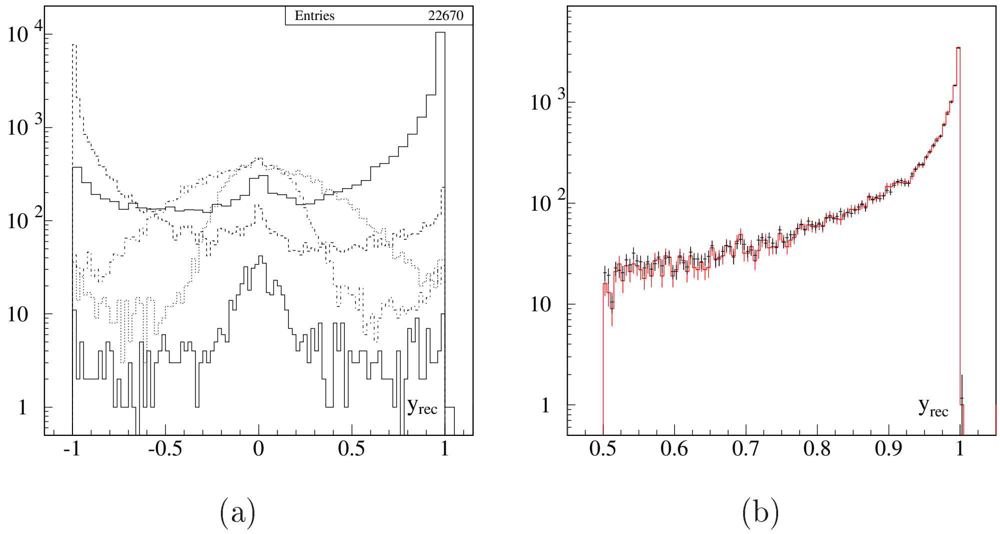

Fig. 13. (a) Monte Carlo: y_{rec} distribution for signal (solid, high statistic) and all background sources (dashed plus solid low statistic); (b) Comparison Data-Monte Carlo for signal

at $y_{rec} > 0.8$ (< -0.8) to select $K_L \to \pi^+ e^- \nu$ ($K_L \to \pi^- e^+ \nu$).

The selection of $e^\pm$ ($\pi^\pm$) events is reinforced by the ToF identification of the corresponding $\pi^\mp$ ($e^\mp$) in the $K_L \to \pi^+ e^- \nu (K_L \to \pi^- e^+ \nu)$ decay. A purity of about 99.5% is obtainded by requiring $|\Delta t_i| < 0.5$ ns.

The contribution of the cluster and track extrapolation efficiencies to the track-to-cluster efficiency have been studied individually. Both the cluster and track extrapolation efficiency have been studied as a function of the particle momenta, the K_L vertex position, impinging angle, and the cluster position (barrel or endcap).

Only the dependence on the particle momentum and on the cluster position have been used for the cluster efficiency and the track extrapolation efficiency. The impact of this assumption has been studied by repeating the evaluation of the efficiency including other dependencies such as the K_L vertex position and the impinging angle. No significant improvement has been observed indicating that the relevant kinematic distribution of the control sample is not biased by the selection.

The efficiencies have been evaluated separately for the 14 run-periods both for data and Monte Carlo. A set of 168 particle momentum dependent efficiency have been produced for data and Monte Carlo, corresponding to different particle type, $e^{\pm}$ and $\pi^{\pm}$, and to different detector type, barrel and endcap. The data Monte Carlo ratio of the efficiency measured on the control samples is used to correct the Monte Carlo evaluation.

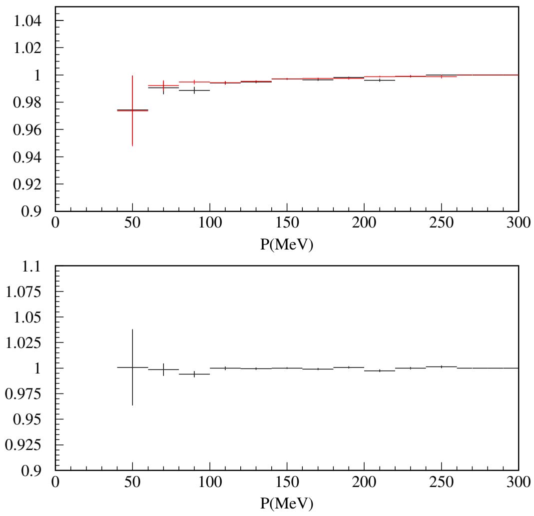

Fig. 14. Top: Cluster efficiency for electron on the barrel from control sample for data (black) and MC (red). Bottom: data Monte Carlo ratio. The plots refer to a single period.

For electrons and positrons the correction results to be small (Fig. 14), while for pions can be large as 30%, and it is different for π^- and π^+, (Fig. 15). Fig. 16 shows the correction as a function of t obtained from a single run-period.

It is worth to stress that if this correction were not taken into account the effect on λ'_+ would be large, about 20%, and would produce a different result for the two charges, about 15%. For this reason the analysis will be performed separately for each charge. The comparison of the two results is first check of the validity of the corrections.

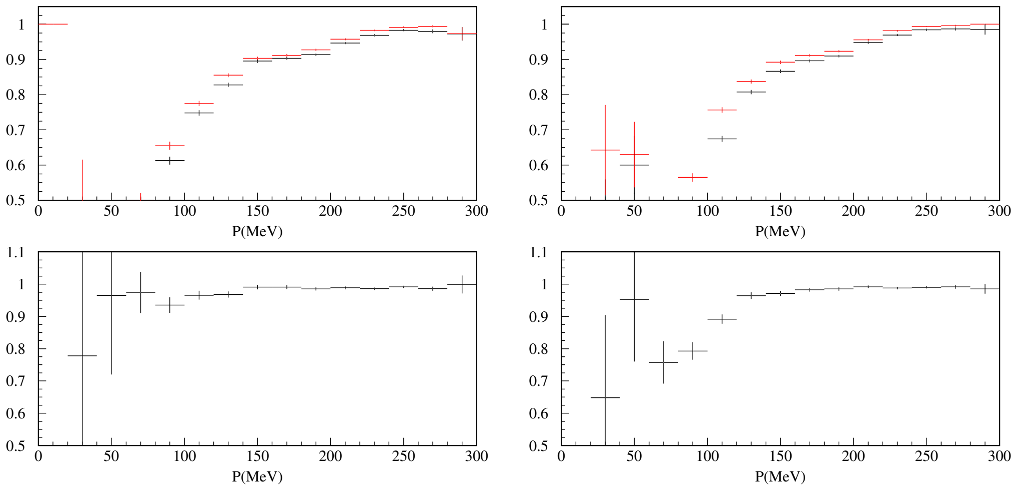

(a) (b)

Fig. 15. Top: Cluster efficiency from control sample for data (black) and Monte Carlo (red). Bottom: data Monte Carlo ratio. For π^- (a) and π^+ (b) The plots refer to a single period.

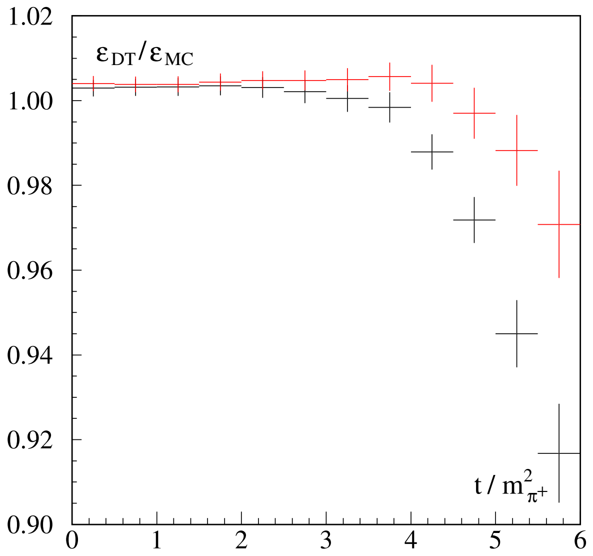

Fig. 16. Cluster efficiency correction for pions (π^- in red, π^+ in black) on the end cap from control sample. The plot refers to a single period.

3.4 ToF efficiency

ToF efficiency is taken from a Monte Carlo with corrections in the time response of the calorimeter taken from control samples (Ref. 2). The data and Monte Carlo distribution of Δt_e and Δt_π are shown in Fig. 17 for events selected as described in Sec. 2.2 or Sec. 3.3. The agreement is adequate for our purpose.

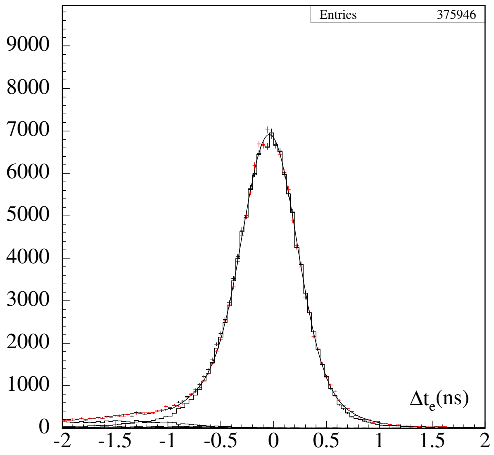

(a)

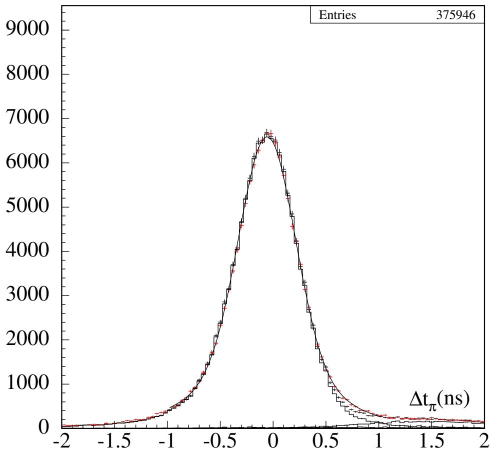

(b)

Fig. 17. Δt_i for electron (a) and pion (b) for data (black) and Monte Carlo (red)

4 Fit function

After background subtraction, we make a t-normalized binned analysis, in which the kinematic range of t/m^2, from $(m_e/m)^2 \sim 0$ up to $(M-m)^2 \sim 6.8$, is enlarged to [-3,7] to include smearing effect. With this choice the fraction of overflow events is $\sim 0.1\%$. In order to fit the rate distribution we use the following formula:

$$\frac{dN}{dt}(i) = N_0 \sum_{j=1}^{20} A(i,j) \times \ \rho(j, \lambda'_+, \lambda''_+) \times \ \epsilon_{tot}(j) \times \ F_{FSR}(j) \tag{9}$$

with $A(i,j)$ being the smearing matrix: the $j^{\text{th}}t$-bin has a not-zero probability to fall into the $i^{\text{th}}t$-bin, with $i \neq j$. The bin size has been set to about 1.6 σ_t, where σ_t is the t resolution. In Fig. 18 is shown the scatter plot of the $j^{\text{th}}t$-bin (reconstructed) versus the $i^{\text{th}}t$-bin (truth). F_{FSR} is the correction to the 'bare' $K_L \to \pi^{\pm}e^{\mp}\nu$ decay due to the final state radiation (see next section). The total efficiency, $\epsilon_{tot}(t)$, takes into account the acceptances and the efficiency of the analysis cuts. The slopes λ'_+ and λ''_+ are free parameters in the fit while the N_0 constant is normalized to the total number of signal counting.

A different approach for the fit procedure has been proposed in Ref. 3.

4.1 Final State Radiation

We cannot neglect the photon emission in the final state. It affects the t-distribution mainly for high energy value of pion, *i.e.* for low t, in which the

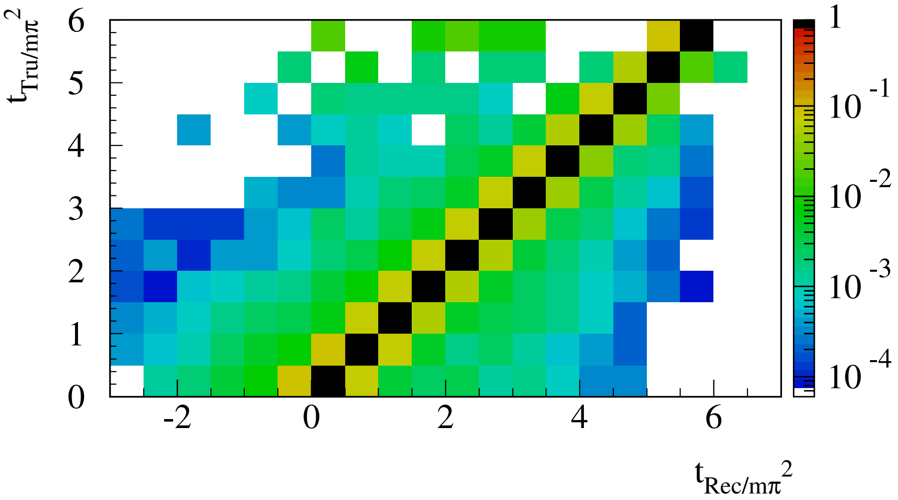

Fig. 18. Scatter plot of the $t_{tru.}$ versus the $t_{Rec.}$

correction is at level of 3-5%. We use the KLOE Monte Carlo simulation, GEANFI [4], to consider the FSR effect [5, 6]. In Fig. 19 the t-distribution with and without FSR are shown. The ratio of these distributions is included in our fit function.

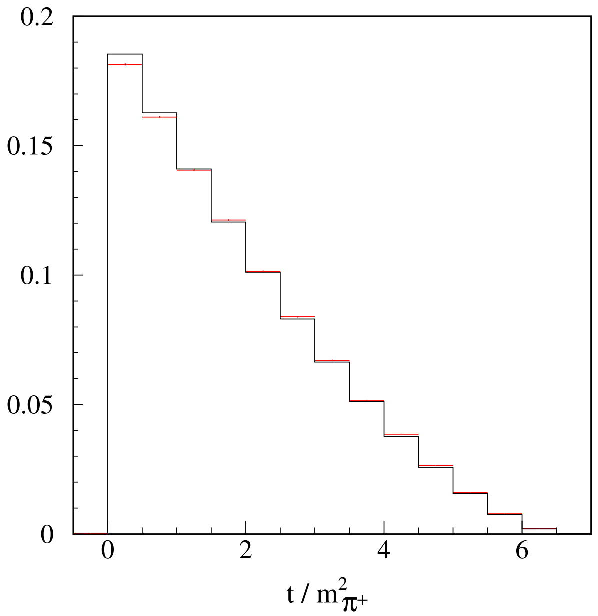

Fig. 19. t-distribution for $K_L \to \pi^{\pm} e^{\mp} \nu$ with(red) and without(black) FSR.

5 Systematic uncertainties

The systematic errors due to the uncertainties in the evaluation of corrections, data-Monte Carlo inconsistencies, result stability, background contamination, and momentum mis-calibration are summarized in Table 1.

	Linear fit	Quadratic fit	
Source	$\delta\lambda'_+ \times 10^3$	$\delta\lambda'_+ \times 10^3$	$\delta\lambda''_+ \times 10^3$
Tag	0.14	0.18	0.02
Trk-Vtx	0.16	0.22	0.18
Tca-Clu	0.07	0.24	0.13
Tof	0.29	0.87	0.27
Bkg	0.08	0.16	0.03
P-scale	0.06	0.05	0.05
P-reso.	0.17	0.22	0.19
Total Syst	0.42	0.98	0.39

Table 1
Summary of systematic uncertainties on λ'_+, λ''_+.

The systematic uncertainties due to the limited knowledge of the tracking and clustering efficiency corrections have been evaluated by checking stability of the result when the selection of tracks and clusters is modified. The validity of the method has been proved by comparing the efficiencies from data control sample, Monte Carlo control sample and Monte Carlo truth(Ref. 2). For data and Monte Carlo samples the efficiency is evaluated from single particle efficiency obtained from control samples (Sec. 3.2 and Sec. 2.2). The corrected efficiency is given by:

$$\epsilon_{MC} \times \frac{\epsilon_{DT}^{cs}}{\epsilon_{MC}^{cs}} \tag{10}$$

The same result should be obtained by correcting the inefficiency :

$$(1 - \epsilon_{MC}) \times \frac{1 - \epsilon_{DT}^{cs}}{1 - \epsilon_{MC}^{cs}} \tag{11}$$

This is valid for vanishing values of ζ_{syst}:

$$\zeta_{syst} = \frac{(\epsilon_{MC}^{cs} - \epsilon_{DT}^{cs}) \times (\epsilon_{MC}^{cs} - \epsilon_{MC})}{\epsilon_{MC}^{cs}(1 - \epsilon_{MC}^{cs})} \tag{12}$$

The value of $\zeta_{syst}(t)$ is used to evaluate the systematic uncertainty. A very similar method has been used also in Ref. 1.

5.1 Tag

The tag selection can induce a slope in the t-distribution. The usual requirement is the *autotrigger*. To evaluate the systematic due to this choice we repeat the measurement without the requirement of *autotrigger*. Corresponding change of 0.14×10^{-3} is observed for λ'_+ in the case of the linear fit, and changes of 0.18×10^{-3} and 0.02×10^{-3} are observed for λ'_+ and λ''_+ respectively in the case of quadratic fit.

5.2 Tracking and vertexing

The uncertainty on the tracking efficiency correction is dominated by sample statistics and by the variation of the results observed using different criteria to identify good tracks from K_L decays. The correction is run-period dependent; its statistical error has been included in the fit.

The effect of differences in the resolution with which the variable $d_{\rm c}$ is reconstructed (Sec. 2.3)in data and in Monte Carlo, and the possible bias introduced in the selection of the control sample, has been studied by varying the values of the cuts made on this variable when associating tracks to K_L vertexes. A total of 5 configurations have been studied. In particular, the cut on $d_{\rm c}$ is illustrated in Fig. 20; the intercept of the line in the figure was varied from 1 cm to 4 cm. These variations resulted in a change of the tracking efficiency of about $\pm15\%$. For each configuration, the complete tracking-efficiency correction was obtained and used to evaluate the slopes. Corresponding change of 0.16×10^{-3} is observed for λ'_+ in the case of the linear fit, and changes of 0.22×10^{-3} and 0.18×10^{-3} are observed for λ'_+ and λ''_+ , respectively, in the case of quadratic fit. Fig. 21 shows the tracking efficiency as function of t for Monte Carlo for three cases: direct evaluation of efficiency from Monte Carlo, denoted as MC truth; evaluation of the efficiency obtained by folding the Monte Carlo kinematics with Monte Carlo control sample efficiency, denoted as MC sample; evaluation of the efficiency obtained by folding the Monte Carlo kinematics with data control sample efficiency, denoted as data sample.

The combined efficiencies obtained from the Monte Carlo and data sample are shown in Fig. 21 (Top), together with the efficiency obtained from Monte Carlo signal. The efficiencies obtained from control samples are in a good agreement, leading to a small value of ζ, as shown at the bottom of the Fig. 21. This value result to be much smaller than the changes observed by varying

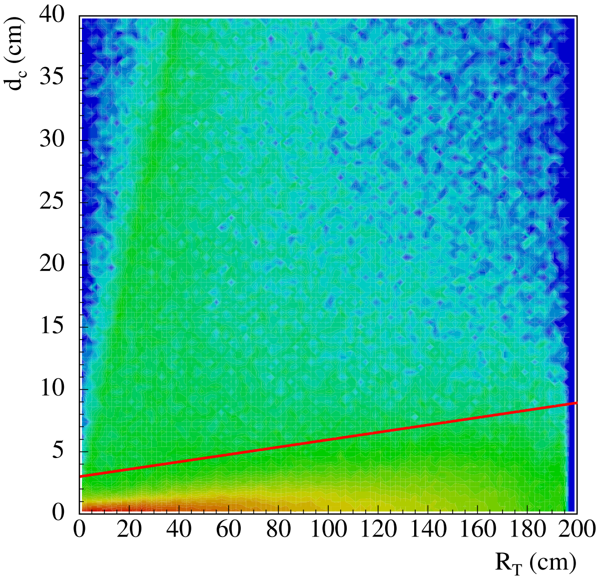

Fig. 20. Scatter plot, d_c vs r_{xy}

the cut on d_c. However, we assume conservatively the changes in the result observed by varying the cut on d_c as systematic uncertainty. The difference observed between the Monte Carlo signal and the sample efficiencies is due to the correlation between the two tracks: the probability to reconstruct the second track given the reconstruction of the first one, is higher. We checked this assumption by counting the fraction of Monte Carlo signal events with zero, one, or two reconstructed tracks. We parametrized the three probabilities as:

$$\begin{aligned} p(0) &= (1 - p_{trk})^2 - \rho \times p_{trk}^2 \\ p(1) &= 2p_{trk} \times (1 - (1 - \rho) \times p_{trk}) \\ p(2) &= p_{trk}^2 \times (1 - \rho) \end{aligned} \qquad (13)$$

where p_{trk} is the single track reconstruction probability, $(1 - \rho) \times p_{trk}$ is the single track conditional probability, and $p(N)$ is the probability to reconstruct N tracks. Using these formula we obtained $(1 - \rho) = 1.069$ and $p_{trk} = 0.711$. Since the sample efficiencies are obtained as a product of two conditional probabilities, we have:

$$p(2)_{sample} = [p_{trk} \times (1 - \rho)]^2 = p(2) \times (1 - \rho) \qquad (14)$$

which corresponds to about $50\% \times 7\% \sim 3\%$ absolute difference between the Monte Carlo truth and sample efficiencies. This is in agreement with what is observed in Fig. 21.

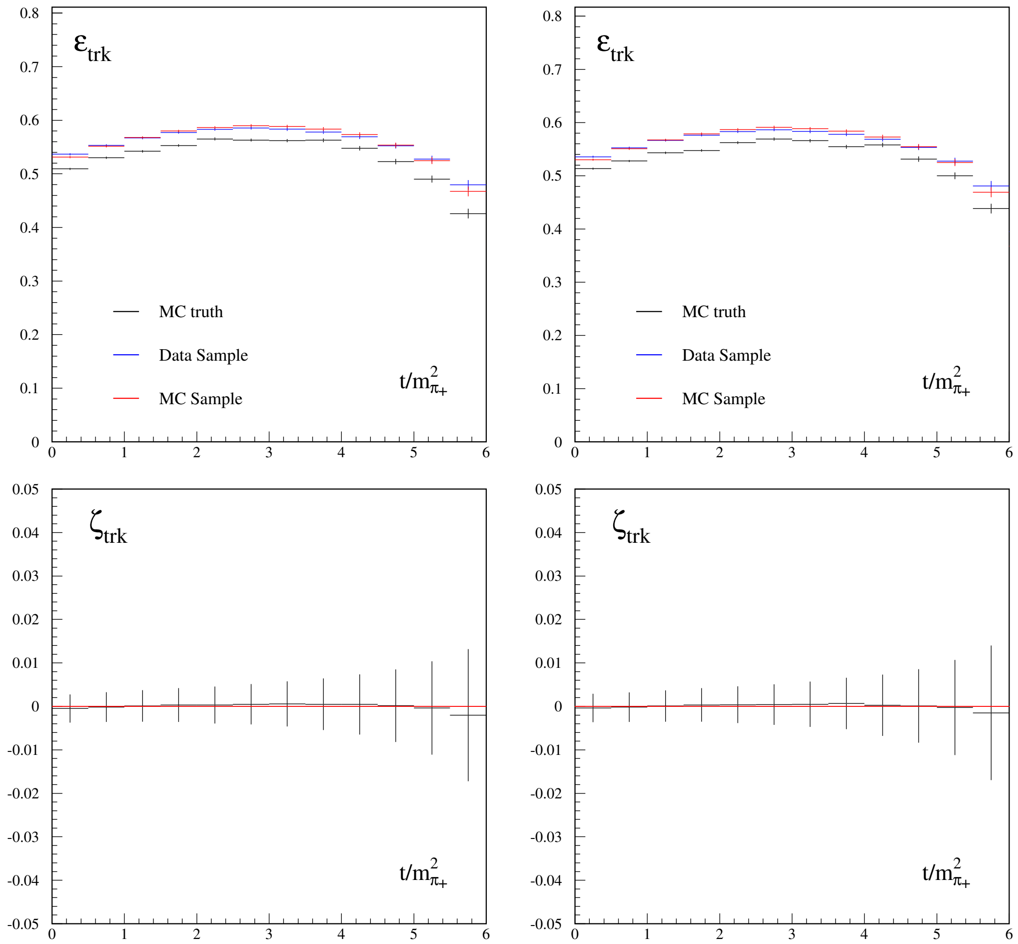

Fig. 21. Top: Tracking and vertexing efficiency as a function of t for data and MC sample, and MC truth. Bottom: ζ as a function of t, for $K_L \to \pi^+ e^- \nu$ (left), and $K_L \to \pi^- e^+ \nu$ (right).

5.3 Track extrapolation and clustering

The uncertainty on the clustering and track extrapolation efficiency correction is dominated by sample statistics and by the variation of the results observed using different criteria for the cluster association. The correction is run-period dependent; its statistical error has been included in the fit.

The most effective variable in the definition of track-to-cluster association is the transverse distance, $\mathrm{d}_{\mathrm{tc}\perp}$, the component of the impact point-centroid distance in the plane transverse to the momentum of the track at impact point. The distribution of this variable is shown in Fig. 3 for Monte Carlo events. The cut on $\mathrm{d}_{\mathrm{tc}\perp}$ has been varied in a wide range from 7 cm to 30 cm, corresponding to a change in efficiency of about 17%. For each configuration, the complete track extrapolation and clustering efficiency correction was obtained and used to evaluate the slopes. Corresponding change of 0.07×10^{-3} is observed for

λ'_+ in the case of the linear fit, and changes of 0.24×10^{-3} and 0.13×10^{-3} are observed for λ'_+ and λ''_+ ,respectively, in the case of quadratic fit.

The second alternative method has been used to evaluate directly the systematic error. Fig. 22 and Fig. 23 show the track extrapolation and the clustering efficiencies as a function of t for Monte Carlo in three cases: MC truth, MC sample, and data sample. A slope of about 1×10^{-3} in the dependence of ζ

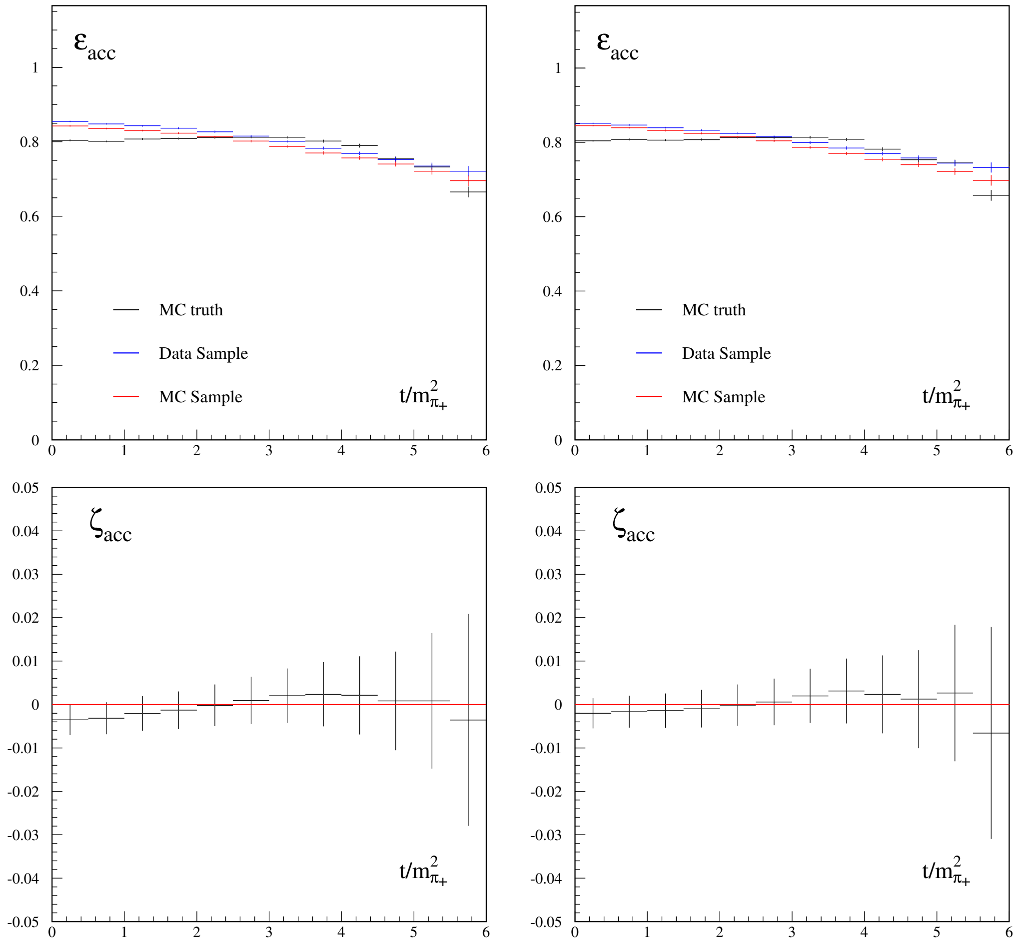

Fig. 22. Top: Track extrapolation efficiency as a function of t for data and MC sample, and MC truth. Bottom: ζ as a function of t. For $K_L \to \pi^+e^-\nu$ (left), and $K_L \to \pi^-e^+\nu$ (right).

from t cannot be excluded in the case of the track extrapolation efficiency(see Fig. 22 bottom). It would translates in a $\sim$ 2% error and $\sim$ 1% error, respectively, on λ'_+ and λ''_+. Also in the case of the cluster efficiency a slope in the dependence of ζ from t cannot be excluded. In this case we have about -1×10^{-3} as shown in Fig. 23. The behavior of ζ as function of t for these two efficiencies is anti-correlated, resulting in a negligible effect on the combined efficiency. In any case the individual contribution give an evaluation of the systematic uncertainty on λ'_+ that is comparable to the result observed by varying the cut on $\mathrm{d}_{\mathrm{tc}\perp}$ and a much smaller systematic on λ''_+.

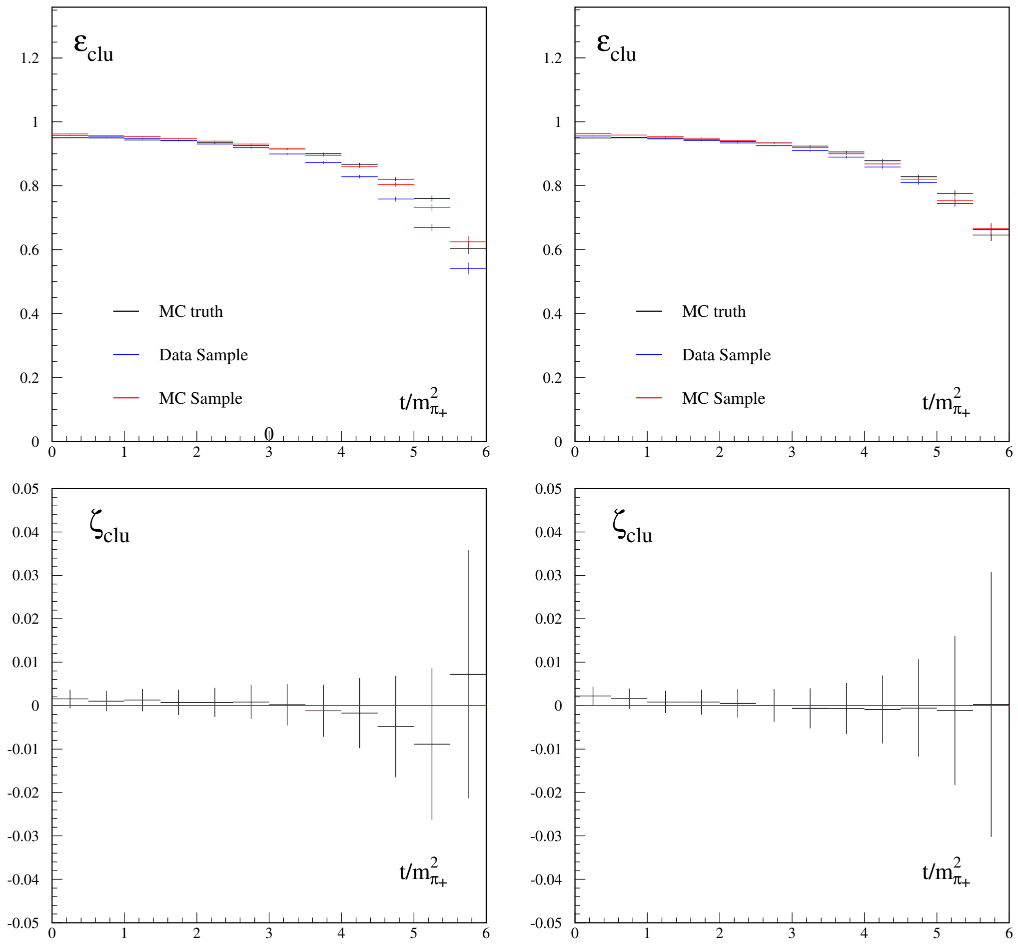

Fig. 23. Top: Track to cluster efficiency as a function of t for data and MC sample, and MC truth. Bottom: ζ as a function of t, for $K_L \to \pi^+ e^- \nu$ (left), and $K_L \to \pi^- e^+ \nu$ (right).

5.4 Tof systematics

The uncertainty on the time of flight selection efficiency has been studied using a pure K_{e3} control sample. The control sample has been selected with the kinematic cut $y_{rec} > 0.8$. The calorimeter particle identification described in Ref. 1 has been used to further reduce the background. The discrimination is based on energy deposition signatures. The energy deposited and the position of the cluster centroid as a function of the particle momentum have been combined using a neural network (NN). Fig. 24 shows the NN output distribution for signal and background, while Fig. 25 shows data Monte Carlo comparison for positive and negative electrons. We require both the NN output to be consistent with the expected particle type $PID > 0.5$ for the negative(positive) charge and $PID < 0.5$ for the positive(negative) charge to select Ke3- (Ke3+). The final contamination of the control sample amount to 0.4%.

A new ToF efficiency has been evaluated using this control sample for the data and Monte Carlo, and the data Monte Carlo ratio has been used to correct the Monte Carlo efficiency [1].

A change in the result of 0.29×10^{-3} for λ'_+ in the case of the linear fit, and a change of 0.87×10^{-3} and 0.27×10^{-3} for λ'_+ and λ''_+ , respectively, in the case of quadratic fit has been found if the new ToF efficiency is used. The variation is well within the statistical uncertainty.

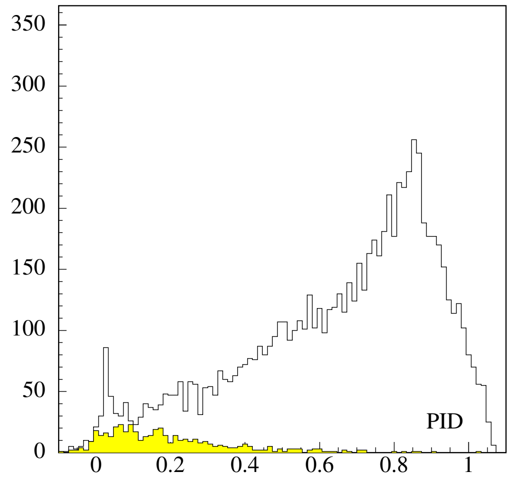

Fig. 24. NN output distribution from Monte Carlo for signal(solid) and background(dashed).

5.5 Background evaluation

The uncertainties on the background evaluation have been studied by repeating the measurement on a sample with a reduced background contamination. The background has been reduced with the identification of the electron using the NN (see Sec. 5.4). Fig. 26 shows the distribution of the NN output for the sample used in the analysis. The background contamination has been reduced by about a factor of three requiring $PID > 0.4$.

The difference in the result obtained with this cut configuration are 0.08×10^{-3} for λ'_+ in the case of the linear fit, and a change of 0.16×10^{-3} and 0.03×10^{-3} for λ'_+ and λ''_+ , respectively, in the case of quadratic fit.

[1] The ToF corrections cannot be used directly in the analysis because of the correlation between the energy response in the calorimeter used in the NN and the ToF.

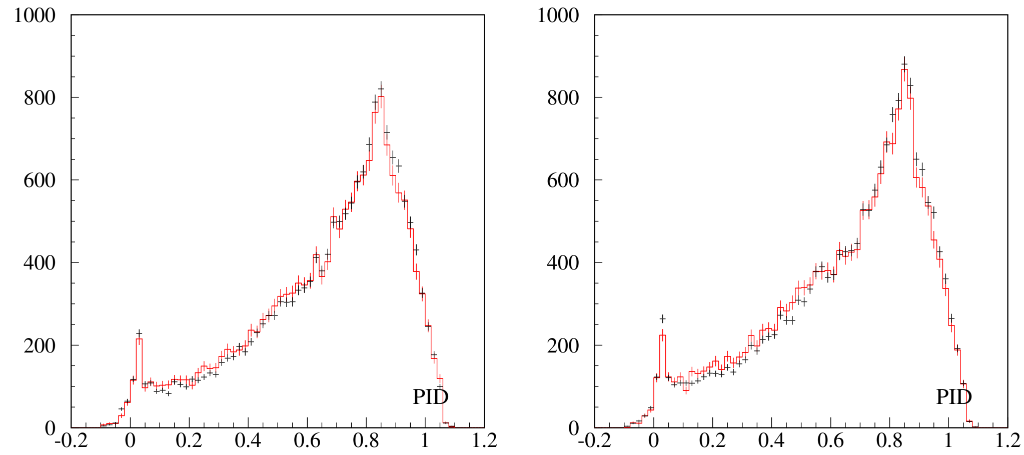

(a) (b)

Fig. 25. Comparison data Monte Carlo. (a) NN output for e^+, (b) NN output for e^-

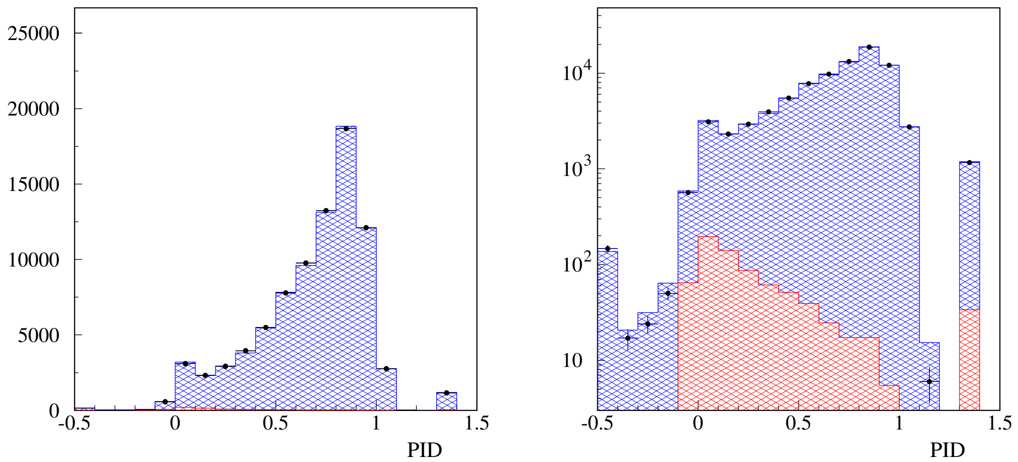

(a) (b)

Fig. 26. NN output distribution for data and Monte Carlo signal (blue hatched) and background (red hatched), in linear (a) and logarithmic scale (b).

5.6 Momentum scale and resolution

The limited knowledge on the momentum scale and the momentum resolution have been considered. We found the following relations by changing the momentum scale:

$$\frac{\delta\lambda'_+}{\lambda'_+} = -2\frac{\delta p}{p}$$

$$\frac{\delta\lambda''_+}{\lambda''_+} = -4\frac{\delta p}{p}$$

We have conservatively assumed a momentum scale uncertainty of 0.1%, well above the accuracy obtained with the dedicated analysis [7]. Corresponding changes of 0.06×10^{-3} have been observed for λ'_+ in the case of the linear fit, and of 0.05×10^{-3} and 0.05×10^{-3} for λ'_+ and λ''_+ , respectively, in the case of quadratic fit.

The limited knowledge of momentum resolution has been investigated by changing the value of the t resolution. The data Monte Carlo agreement of several variables that are sensitive to the momentum resolution has been studied in Ref. 1. The examples of Fig. 2.4, Fig. 12, and Fig. 3.3, show a good data Monte Carlo agreement. A variation of the t resolution of 3% worsen the fit quality giving a χ^2 probability of about 28%. The corresponding absolute changes are 0.17×10^{-3} for λ'_+ in the case of the linear fit, and of 0.22×10^{-3} and 0.19×10^{-3} for λ'_+ and λ''_+ in the case of quadratic fit. In principle, if the distribution has a linear behavior, the slope is insensitive to any smearing due to the resolution. The only effect is due to the depletion of the bins at the boundary of the distribution, which worsen the χ^2 of the fit. In fact, we checked that the sensitivity to the momentum resolution is much smaller for a reduced fit range. A higher variation of the t resolution of 6% gives an unacceptable χ^2 probability, about 10^{-9}, with almost the same variations for the fit parameters. We assume as a systematic error the variation obtained for the slope parameters, when the χ^2 probability is lowered to about 30%.

6 Results

Fig. 27 shows the value of λ'_+ as a function of run period. The error bars in Fig. 27 represent only the uncorrelated statical errors [2] for each run period. Good stability of the results is observed once the efficiency corrections for each run period are applied. In particular, the fit has been performed separately for $K_L \to \pi^+ e^- \nu$ and $K_L \to \pi^- e^+ \nu$ to check the reliability of the cluster efficiency, that has a different value in the two cases. The results are consistent only if the efficiency corrections for each pion charge are applied. The results of the linear fit obtained over all run periods are given in Table 2.

Including the systematic uncertainties shown in Table 1 we have:

$$\lambda'_+ = 28.6 \pm 0.5_{stat.} \pm 0.4_{syst.}$$

[2] These include the statistical uncertainties due to the limited knowledge of the corrections and the effects of finite Monte Carlo statistics.

The results obtained for the quadratic fit are shown in Table 3. A correlation ~ -0.95 between λ'_+ and λ''_+ parameters has been obtained, as expected from form factors parametrization definition in Eq. 2 [8]. Only a mild preference for a small quadratic term is observed as indicated by the slight improvement in the fit probability going from the linear, $\mathrm{P}(\chi^2) = 89\%$, to the quadratic fit $\mathrm{P}(\chi^2) = 92\%$.

Including the systematic uncertainties shown in Table 1 we have:

$$\lambda'_+ = 25.5 \pm 1.5_{stat.} \pm 1.0_{syst.}$$
$$\lambda''_+ = 1.4 \pm 0.7_{stat.} \pm 0.4_{syst.}$$

Fig. 28 and Fig. 29 show the t distribution of data and the fit result for $K_L \to \pi^+ e^- \nu$ and $K_L \to \pi^- e^+ \nu$ respectively. The ratio data fit is also shown.

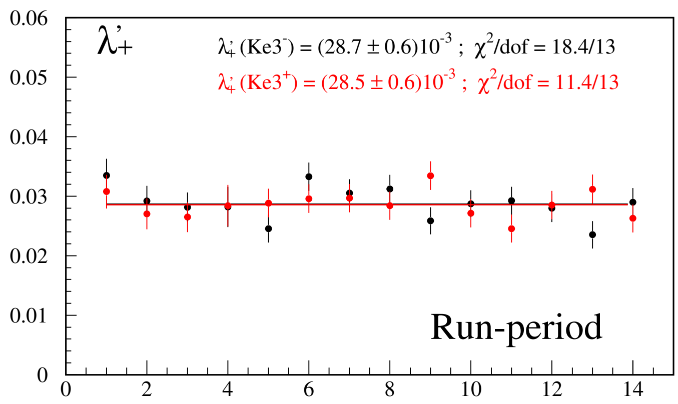

Fig. 27. Linear fit for period and for charge. $K_L \to \pi^+ e^- \nu$ in black, $K_L \to \pi^- e^+ \nu$ in red. The plot refers to all 14 run periods.

Linear fit	$\lambda'_+ \times 10^3$	χ^2/ndf
$K_L \to \pi^- e^+ \nu$	28.7 ± 0.7	$156/181$
$K_L \to \pi^+ e^- \nu$	28.5 ± 0.6	$174/181$
Combined	28.6 ± 0.5	$330/363$

Table 2
Fit results in the hypothesis λ''_+=0.

We have also fit the data using the one pole parametrization (see Eq. 1). We obtain $M_V = (870 \pm 6)$ with $\chi^2/ndf = 326/364$ and a probability of $\mathrm{P}(\chi^2) = 92.4\%$. Taking into account also the systematic error we get:

$$M_V = (870 \pm 6_{stat.} \pm 7_{syst.})\ \mathrm{MeV}$$

Quadratic fit	$\lambda'_+ \times 10^3$	$\lambda''_+ \times 10^3$	χ^2/ndf
$K_L \to \pi^- e^+ \nu$	24.6 ± 2.1	1.9 ± 1.0	$152/180$
$K_L \to \pi^+ e^- \nu$	26.4 ± 2.1	1.0 ± 1.0	$173/180$
Combined	25.5 ± 1.5	1.4 ± 0.7	$325/362$

Table 3
Fit results with λ'_+ and λ''_+ as free parameters.

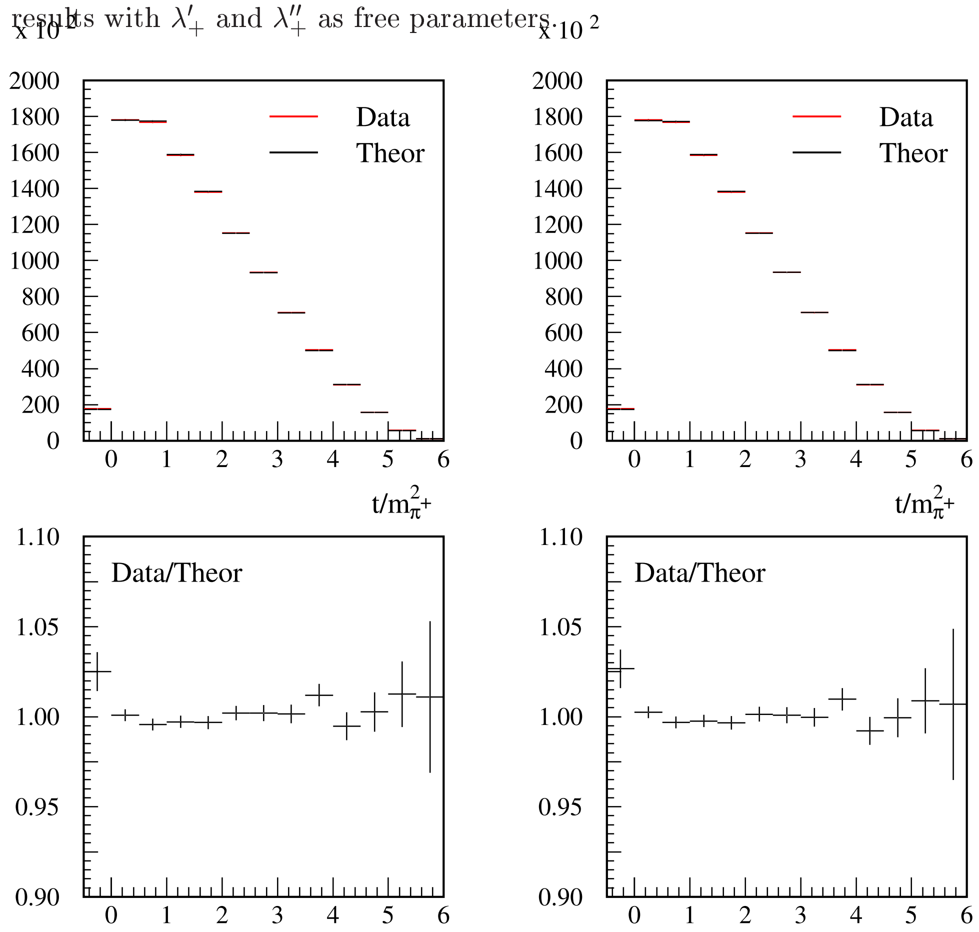

(a) Linear fit (b) Quadratic fit

Fig. 28. Fit results for $K_L \to \pi^+ e^- \nu$: data(red) are superimposed to fit function (black). Data/Fit ratio is also shown.

in marginal agreement with the mass of the K* vector meson indicating the presence of other contributions like the non resonant $K\pi$ scattering.

Conclusion

We have obtained new, precise values of the slopes used to describe the hadronic from factor in the K_{e3} decay. The new KLOE result is consistent

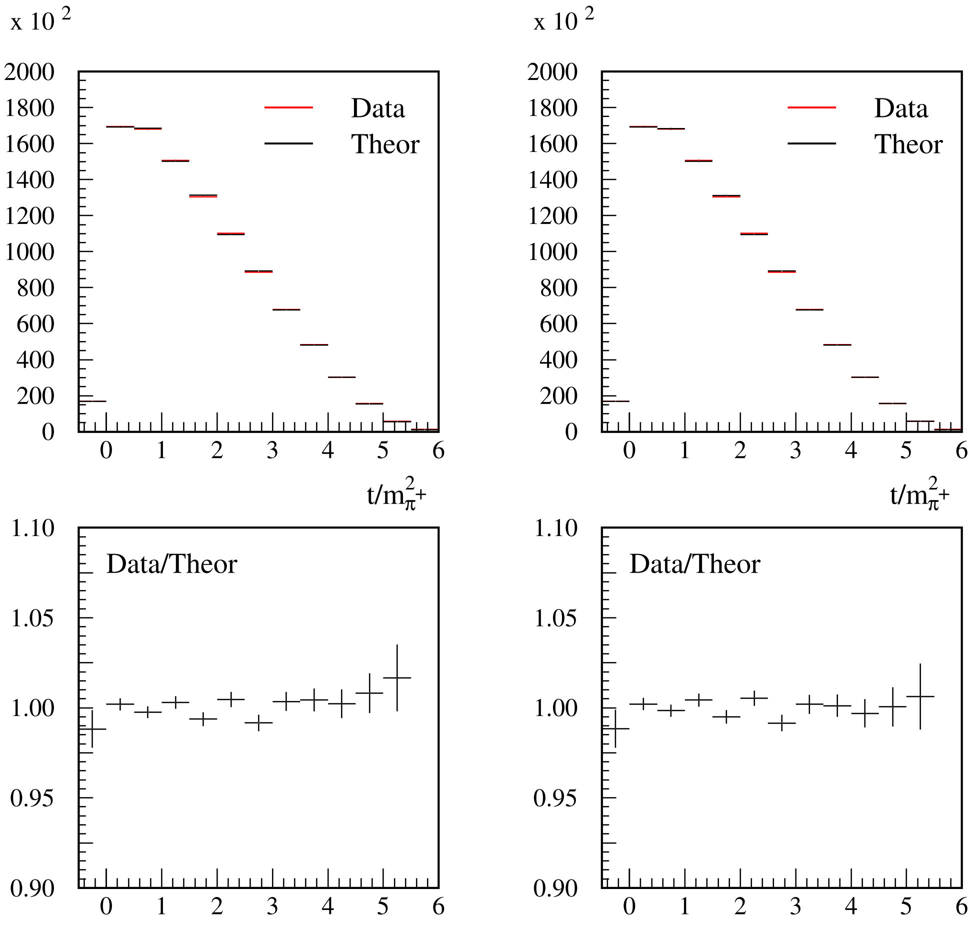

(a) Linear fit (b) Quadratic fit

Fig. 29. Fit results for $K_L \to \pi^- e^+ \nu$: data(red) are superimposed to fit function (black). Data/Fit ratio is also shown.

with the presence of a small quadratic term in agreement with the expectation of one pole expansion. The comparison with other existing measurements is shown in Fig. 30. It can be seen that the value of λ'_+ obtained with the linear fit is in good agreement with other existing measurements. In the case of the quadratic fit our result is in good agreement with ISTRA+ ([9]), after correcting for the fact that they use the neutral pion mass in their expansion of the form factor. Our result falls almost half way between and NA48 ([10]) and in marginal disagreement with KTeV ([11]).

References

[1] M. Antonelli, P. Beltrame, M. Dreucci, M. Moulson, M. Paultan, A. Sibidanov, Measurements of the absolute branching ratios for dominant K_L decays, the K_L lifetime, and v_{us} with the kloe detector, KLOE Note 204 (2005).
URL http://www.lnf.infn.it/kloe/pub/knote/kn204.ps.gz

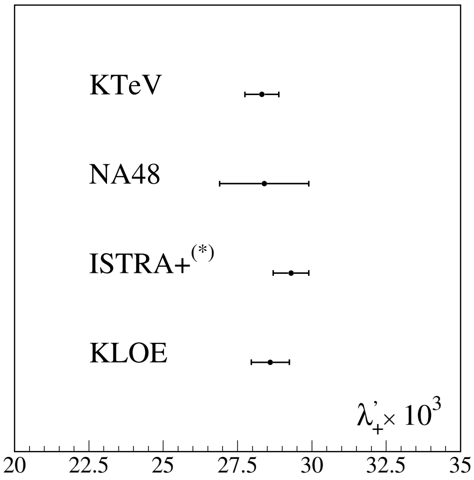

(a) Linear fit

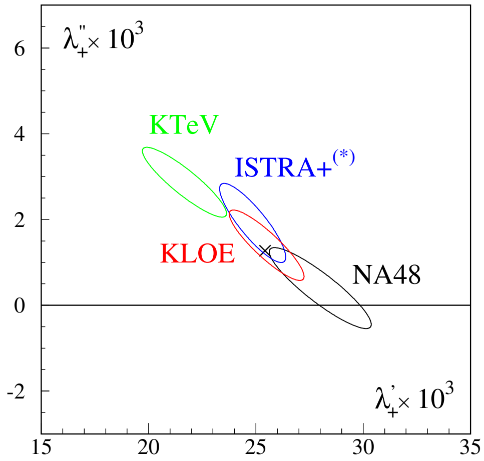

(b) Quadratic fit

Fig. 30. Comparison with other published results. The cross in (b) represents λ'_+ and λ''_+ obtained from the Taylor expansion of the pole parametrization. (*) The ISTRA+ result have been multiplied by the factor $(m_{\pi^+}/m_{\pi^0})^2$.

[2] C. Gatti, T. Spadaro, Measurement of the branching fraction and the charge asymmetry for the decay BR($K_S \to \pi e \nu$), KLOE Memo 318 (2005). URL http://www.lnf.infn.it/kloe/pub/kmemo/km318.ps.gz

[3] G. Capon, Comment on parameter fitting for k/η decay into 3 pions or ke3 form factor, KLOE Memo 317 (2005). URL http://www.lnf.infn.it/kloe/pub/kmemo/km317.ps.gz

[4] F. Ambrosino, et al., Data handling, reconstruction, and simulation for the KLOE experiment, Nucl. Instrum. Meth. A 534 (2004) 403.

[5] C. Gatti, MC generators for radiative kaon decays, KLOE Note 194 (2004). URL http://www.lnf.infn.it/kloe/pub/knote/kn194.ps

[6] C. Gatti, Monte Carlo simulation for radiative kaon decays, hep-ph/0507280, accepted by Eur. Phys. J. C .

[7] A. Antonelli, et al., The KLOE field map revisited, KLOE Memo 233 (2001).

[8] P. Franzini, Slope parameters of k→pi form factor, KLOE Memo 312 (2005). URL http://www.lnf.infn.it/kloe/pub/kmemo/km312.ps.gz

[9] O. P. Yushchenko, et al., Phys. Lett. B 589 (2004) 111.

[10] NA48 Collaboration, A. Lai, et al., Phys. Lett. B 606 (2004) 1.

[11] KTeV Collaboration, T. Alexopolous, et al., Phys. Rev. D 70 (2004) 092007.